

# Narrow photoluminescence peak of epitaxial MoS<sub>2</sub> on graphene/Ir(111)

Niels Ehlen<sup>1</sup>, Joshua Hall<sup>1</sup>, Boris V. Senkovskiy<sup>1</sup>, Martin Hell<sup>1</sup>, Jun Li<sup>1</sup>, Alexander Herman<sup>1</sup>, Dmitry Smirnov<sup>2</sup>, Alexander Fedorov<sup>1,2,3</sup>, Vladimir Yu. Voroshnin<sup>2,3</sup>, Giovanni di Santo<sup>4</sup>, Luca Petaccia<sup>4</sup>, Thomas Michely<sup>1</sup>, Alexander Grüneis<sup>1</sup>

<sup>1</sup> II. Physikalisches Institut, Universität zu Köln, Zùlpicher StraÙe 77, 50937 Köln, Germany

<sup>2</sup> Helmholtz-Zentrum Berlin für Materialien und Energie, Elektronenspeicherring BESSY II, Albert-Einstein-StraÙe 15, 12489 Berlin, Germany

<sup>3</sup> IFW Dresden, HelmholtzstraÙe 20, 01069 Dresden, Germany

<sup>4</sup> Elettra Sincrotrone Trieste, Strada Statale 14 km 163.5, 34149 Trieste, Italy

**Abstract.** We report on the observation of photoluminescence (PL) with a narrow 18 meV peak width from molecular beam epitaxy grown MoS<sub>2</sub> on graphene/Ir(111). This observation is explained in terms of a weak graphene-MoS<sub>2</sub> interaction that prevents PL quenching expected for a metallic substrate. The weak interaction of MoS<sub>2</sub> with the graphene is highlighted by angle-resolved photoemission spectroscopy and temperature dependent Raman spectroscopy. These methods reveal that there is no hybridization between electronic states of graphene and MoS<sub>2</sub> and a different thermal expansion of graphene and MoS<sub>2</sub>. Molecular beam epitaxy grown MoS<sub>2</sub> on graphene is therefore an important platform for optoelectronics which allows for large area growth with controlled properties.

## 1. Introduction

Following in the wake of graphene research, the optical properties of monolayer MoS<sub>2</sub> and related materials have stimulated intense research efforts over the last years [1, 2, 3]. The MoS<sub>2</sub> monolayer can take the form of 2H or 1T (1T') crystal structures [4], with the 2H phase being a two-dimensional semiconductor with a direct band gap that exhibits photoluminescence [1]. Research has shown promise for applications of MoS<sub>2</sub> as field effect transistors, electroluminescent devices [5, 6] and in the area of spintronics [7]. However, most progress in our understanding of this material is still based on exfoliated layers, e.g. the recently observed record narrow luminescence of 5 meV [8]. Small flake size and the inherent inability of exfoliation for scale up impedes not only scientific research using methods where a large area film with a single orientation is needed. It also precludes the development of MoS<sub>2</sub> based electronics. A clean and scalable approach to MoS<sub>2</sub> and other transition metal dichalcogenide synthesis is very low pressure chemical vapour deposition (CVD) using a catalytically active metallic substrate to support the decomposition of a sulphur containing precursor molecule. For example, simultaneous supply of Mo and H<sub>2</sub>S molecules yields large islands and even single domain monolayer coverage of MoS<sub>2</sub> on Au(111) [9, 10]. However, the substantial interaction and hybridization of the layer with the metallic substrate modifies the properties of the layer substantially. This is a drawback specifically when considering potential applications in optics. Due to the low reactivity of van der Waals substrates like graphene or hexagonal boron nitride, neither phase pure layers nor a well defined epitaxial relation could be realized up to now with such sulphur containing precursor molecules [11]. Through molecular beam epitaxy (MBE) using elemental sulphur – supplied e.g. from a valved sulphur cracker cell or from a Knudsen cell releasing elemental sulphur out of a compound like FeS<sub>2</sub> – phase pure and epitaxial transition metal disulfide layers could be grown even on van der Waals substrates to which they are only weakly bonded [12, 13].

However, a complete spectroscopic characterization of such heterostructures is missing so far despite the fundamental interest in MoS<sub>2</sub> on graphene (MoS<sub>2</sub>/Gr) e.g. as a photodetector [14]. Moreover, none of the above mentioned works on MBE grown MoS<sub>2</sub> reported optical (photoluminescence or Raman) characterization of the material. This is surprising because optical methods are a main tool for the investigation of exfoliated MoS<sub>2</sub> [3]. The lack of optical spectroscopy characterization for MBE grown MoS<sub>2</sub> might be explained by the fact that these methods are less prevalent in the MBE community.

The present manuscript addresses these points and, besides structural investigation, investigates MBE-grown MoS<sub>2</sub> spectroscopically using X-ray photoemission spectroscopy (XPS), angle-resolved photoemission spectroscopy (ARPES) and optical (Raman and luminescence) methods. For the monolayer islands of MoS<sub>2</sub> epitaxially grown on a closed layer of graphene on Ir(111), as seen by scanning tunneling microscopy (STM) and low energy electron diffraction (LEED), the band structure measured by ARPES highlights the absence of any hybridization between MoS<sub>2</sub> and graphene. Our results reveal that the photoluminescence (PL) of MoS<sub>2</sub>/Gr/Ir(111) is present despite

the metallic substrate. We compare the optical bandgap obtained from PL measurements of the pristine MoS<sub>2</sub>/Gr/Ir(111) system to the energy separation between valence and conduction bands of the lithium (Li) doped system that we measured using ARPES. By careful analysis of this data and taking into account the doping induced bandgap renormalization, we estimate an exciton binding energy of 480 meV. The temperature dependence of the bond lengths in graphene and MoS<sub>2</sub> is probed using Raman spectroscopy. We find that the lattice expansion of graphene and MoS<sub>2</sub> behave completely different. Graphene's lattice expansion is dictated by the underlying Ir. The layer of MoS<sub>2</sub>, which is not in direct contact to the Ir(111), roughly follows the lattice expansion expected for freestanding MoS<sub>2</sub>. Our findings introduce MBE grown MoS<sub>2</sub>/Gr as a highly ordered, epitaxial heterostructure with a sharp optical emission that can be grown in large scale.

## 2. Experimental Results

### 2.1. Structure and electronic properties

Prior to the analysis of the electronic and optical properties of the MoS<sub>2</sub> layer, we present in Figure 1 its microscopic, structural and chemical characterization. In (a), a large scale STM topograph of the MoS<sub>2</sub> island layer is shown. The islands rest on the Gr/Ir(111) substrate, which has two monatomic step edges crossing the topograph horizontally. A large fraction of the substrate is covered by monolayer islands (green arrow in the inset), decorated with small bilayer islands (black arrow). On both, the monolayer and the bilayer, a metallic edge state surrounding the islands can be observed (blue arrow), since the bias voltage lies in the band gap of the semiconductor MoS<sub>2</sub>. Bright lines, running across the MoS<sub>2</sub> islands can be identified as (mirror) twin boundaries (white arrow) [15]. The MoS<sub>2</sub> islands are extremely clean with a negligible density of defects. Subfigure (b) displays a LEED pattern of the sample, indicating the epitaxial relation between the substrate and the adlayer. Going from outside to inside, the first order Gr and Ir(111) spots and their associated moiré can be seen. Farthest inside, slightly rotationally broadened first order MoS<sub>2</sub> diffraction spots indicate a lattice constant of  $(3.13 \pm 0.03) \text{ \AA}$ , in line with the literature [16]. To probe the chemical properties, XPS was performed. Figure 1(c) compares the Mo 3d core level of elemental molybdenum in red (produced by evaporating molybdenum onto the Gr/Ir(111) surface without any source for sulfur) to the grown MoS<sub>2</sub>/Gr/Ir(111) structure in green. It can be seen that the Mo 3d core level is shifted to higher binding energy by 0.95 eV. This shift is in line with earlier observations of MoS<sub>2</sub> grown on a gold substrate [17]. In these previous results, a splitting of the Mo 3d core level was observed into three components (low binding-energy, mid binding-energy and high binding-energy component) [17]. In comparison, our Mo 3d peak lacks the reported low binding-energy and mid binding-energy components which are attributed to metallic Mo and Mo on the edge of a flake. For the low binding-energy peak, we attribute this to the fact that all available Mo

[A4] This image shows a series of microscopy and spectroscopy measurements characterizing a material, likely a 2D heterostructure. Let's break down each panel:

"(a) Atomic Force Microscopy (AFM) Image:"

This panel displays an AFM image, a technique that maps surface topography. The image shows a surface with a pattern of hexagonal or near-hexagonal shapes. The scale bar indicates 100 nm. The inset shows a magnified view highlighting the individual shapes and arrows indicating the direction of the crystallographic axes or the orientation of features within the shapes. The color scale represents height; higher areas are higher. The shapes appear to be islands or domains of a material on a substrate.

"(b) Selected Area Electron Diffraction (SAED) Pattern:"

This panel presents a SAED pattern obtained from transmission electron microscopy (TEM). SAED patterns reveal the crystalline structure of a material. The central spot is the transmitted beam. The surrounding spots represent the diffraction of the electron beam from the crystal lattice planes. The image shows diffraction spots characteristic of a crystalline structure. The labels "Gr," "Ir," and "MoS<sub>2</sub>" indicate the presence of graphene (Gr), iridium (Ir), and molybdenum disulfide (MoS<sub>2</sub>). The blue circle highlights a hexagonal pattern, which arises from the superposition of two slightly misaligned hexagons (Gr and Ir in this case), revealing the interaction between the layers.

"(c) X-ray Photoelectron Spectroscopy (XPS) Spectrum (Mo 3d and S 2s):"

This panel presents XPS data, a surface-sensitive technique that probes the chemical composition and electronic states of a material. Two peaks are shown: Mo 3d and S 2s. The presence of two sets of peaks (orange and green) suggests two different chemical environments for molybdenum. The legend indicates that the green peaks correspond to sulfur-bonded molybdenum (sulfurated Mo), while the orange ones correspond to elemental molybdenum. The energy difference (0.95 eV) between the peaks is highlighted, indicating a slight energy shift due to the chemical bonding.

"(d) XPS Spectrum (S 2p):"

This is another XPS spectrum, focusing specifically on the S 2p core level. The single green peak further supports the presence of sulfur in the sample, consistent with the sulfurization of molybdenum (MoS<sub>2</sub>).

"(e) XPS Spectrum (C 1s):"

This XPS spectrum shows the C 1s core level. The peak suggests the presence of carbon, possibly from residual carbon contamination or from the graphene layer.

"Overall Interpretation:"

The data strongly suggest a heterostructure composed of graphene, iridium, and molybdenum disulfide (MoS<sub>2</sub>). The AFM shows the morphology of the MoS<sub>2</sub> domains. The SAED confirms the crystalline structure and shows the moiré pattern from the graphene-iridium interaction. The XPS data indicates the presence of MoS<sub>2</sub> (sulfurated Mo) and elemental Mo, and also confirms the presence of S and C. The energy difference in the Mo 3d peaks in (c) might provide information about the interaction between MoS<sub>2</sub> and the other layers. The combination of these techniques provides a comprehensive characterization of the material's structure, composition, and chemical states. (SMG)

**Figure 1.** (a) Large scale STM topograph of  $\text{MoS}_2$  islands on fully covered  $\text{Gr}/\text{Ir}(111)$  grown in two successive growth cycles (cf. Methods) and subsequently imaged in situ. The inset shows a zoomed in part of the image marked with a blue box. The arrows in the inset mark different features of the topograph. green: monolayer  $\text{MoS}_2$  island, black: bilayer  $\text{MoS}_2$  island, white: mirror twin boundary, blue: metallic edge state. Image information: Tunneling voltage -1.5 V, tunneling current 20 pA, image size  $250 \times 250 \text{ nm}^2$ . (b) Corresponding LEED pattern at 86 eV. (c) XPS spectra of the Mo 3d peak. The doublet peak is split into Mo 3d<sub>5/2</sub> and Mo 3d<sub>3/2</sub> components. The red color traces show the peak for elemental Mo, green color for  $\text{MoS}_2$  which is shifted by 0.95 eV to a higher binding energy. The additional peak in the green spectrum around 226.5 eV binding energy is due to the S 2s core level. The spectra were recorded using an excitation energy of 370 eV. (d) S 2p doublet peak from the grown  $\text{MoS}_2$  using 300 eV excitation energy. (e) XPS Spectra of the C 1s peak using an excitation energy of 370 eV.

was used up in the reaction to form  $\text{MoS}_2$  and no elemental Mo is left over. The absence of the mid binding-energy component can be explained by the large island size

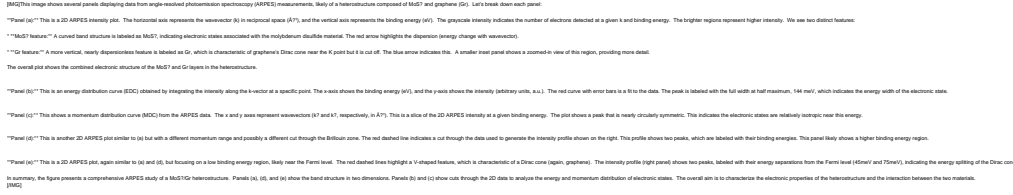


**Figure 2.** (a) ARPES spectra of MoS<sub>2</sub>/Gr/Ir(111) taken with p-polarized light at  $h\nu = 31$  eV and  $T = 20$  K. The inset shows the region around the MoS<sub>2</sub>  $K$  point in high-resolution. An energy distribution curve (EDC) cut of that data at the  $K$ -point of MoS<sub>2</sub> (labelled by  $K_{MoS_2}$ ) is depicted in (b). The extracted spin-orbit splitting is 144 meV. (c) Fermi-surface map of graphene. The blue dot in the Fermi surface map denotes the position of the  $K$  point of graphene and is labelled by  $K_{Gr}$  in (a). We extract a hole density of  $1.484 \times 10^{13} \text{ cm}^{-2}$ . (d) ARPES scan of Li-doped MoS<sub>2</sub>/gr/Ir(111). (e) High resolution scan close to the Fermi level around the  $K$  point of doped MoS<sub>2</sub> shows the conduction band shifting below the Fermi level upon Li evaporation. As a guide to the eye we have inserted a parabola shown in red. EDC cuts through the data are shown to the right of the ARPES scans in blue. A fit to the data is shown in black.

achieved in this work. This increases the “bulk” versus the edge contribution to a point where the edge contribution is negligible. The sulfur 2p peak is shown in Figure 1(d). Our analysis confirms the growth of crystalline MoS<sub>2</sub> and the absence of amorphous MoS<sub>3</sub> [18]. Results of MoS<sub>2</sub> grown on gold show an asymmetry in the S 2p peak [10] compared to the present work. This can be explained by the influence of the gold substrate on the lower sulfur layer. This asymmetry is not visible for MoS<sub>2</sub>/Gr/Ir(111), suggesting a negligible influence of the Gr/Ir(111) substrate on the lower sulfide layer and thus a weak interaction of the substrate with the grown MoS<sub>2</sub> islands. As we will discuss later, this weak interaction is key to observing PL. The C 1s peak of the graphene layer is shown in Figure 1(e).

Figure 2 shows angle-resolved photoemission spectroscopy (ARPES) results of the same system. An overview scan depicting the bands of graphene, MoS<sub>2</sub> and the Ir substrate is shown in Figure 2(a). The  $K$  point of graphene is at  $\sim 1.7 \text{ \AA}^{-1}$  and the  $K$  point of MoS<sub>2</sub> at  $\sim 1.3 \text{ \AA}^{-1}$ , both are indicated at the top x-axis. The valence band

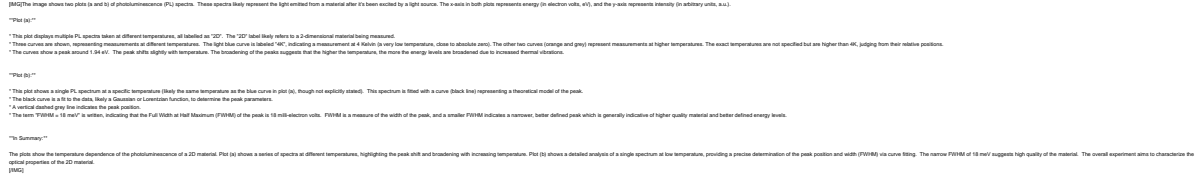
(VB) maximum of MoS<sub>2</sub> appears at the  $K$ -point consistent with monolayer MoS<sub>2</sub>. For comparison, bilayer MoS<sub>2</sub> (shown in the supporting information) has the VB maximum at the  $\Gamma$  point. By taking the distance between the VB maximum of MoS<sub>2</sub> at the  $K$ -point to the Fermi level (approximately 1.5 eV), it suggests that the Fermi level is closer to the conduction band (CB) than to the valence band of MoS<sub>2</sub> as the measured electronic bandgap is typically below 2.6 eV[3]. The splitting of the VB at  $K$  due to spin-orbit interaction is clearly seen in the high resolution scan shown in the inset to Figure 2(a). The fit to the energy distribution curve from a cut through the MoS<sub>2</sub>  $K$ -point is shown in Figure 2(b) and reveals a spin-orbit coupling of 144 meV. Interestingly, graphene is more hole doped than it was before MoS<sub>2</sub> growth, the Dirac-point binding energy is evaluated to be  $E_{Dirac} = -0.25$  eV compared to  $E_{Dirac} = -0.1$  eV in the pristine case [19]. The hole doping can be seen from the ARPES scans and the map shown in Figures 2(a,c). The fact that hole doping increases after performing the MoS<sub>2</sub> growth on Gr/Ir(111) is also evident from a comparison to other works on Gr/Ir(111) [20, 21]. Analysis of the Fermi surface yields a hole concentration of  $1.48 \times 10^{13} \text{ cm}^{-2}$ . As we will see later, this hole doping is also responsible for the shift of the Raman active  $G$  band of Gr. Notably, ARPES does not show any hybridization between MoS<sub>2</sub> and graphene bands which supports the idea that MoS<sub>2</sub> is weakly interacting with Gr.

In order to measure the CB edge using ARPES, we have performed Li doping which induces an electron transfer from Li to the MoS<sub>2</sub> layer thereby populating its CB. Figures 2(d,e) show ARPES spectra of Li doped MoS<sub>2</sub>/Gr heterostructures. The doping turns MoS<sub>2</sub> into a metal which is corroborated from the ARPES observation of a CB at the  $K$  point of MoS<sub>2</sub> (the CB is visible as a parabola at the Fermi level in Figure 2(e)). Assuming a circular Fermi surface of Li-doped MoS<sub>2</sub>, we estimate an electron concentration of  $3.2 \times 10^{13} \text{ per cm}^2$ .

The VB shifts down in energy and broadens but is otherwise unchanged. A Li induced phase transition in MoS<sub>2</sub> has been predicted theoretically [22, 23] and experimentally reported in Li intercalated quantum dots [24]. Interestingly, in the present system we do not observe a structural phase transition of MoS<sub>2</sub> to a 1T (or 1T') phase which would be visible as a different band structure in the ARPES measurements [25, 23]. An energy distribution curve (EDC) through the  $K$  point yields peaks at 75 meV (CB minimum) and 2.05 eV (upper VB maximum). Their difference is equal to 1.975 eV. This value is similar to what has been measured in potassium intercalated monolayer MoS<sub>2</sub> on bulk MoS<sub>2</sub> where 1.86 eV was found [26]. In the next section we compare the obtained VB-CB separation to the energy of the PL to estimate a lower bound of the exciton binding energy.

## 2.2. Luminescent properties

Samples prepared and characterized in this way have then been transferred without exposure to air to an ultra-high-vacuum (UHV) PL/Raman system [27]. Despite the MoS<sub>2</sub> islands are grown on a metallic substrate we were able to detect PL at low



temperatures. Figure 3(a) shows the PL spectra as the sample temperature is lowered. Besides the peak that originates from the PL a second order 2D Raman peak from graphene is seen slightly above 1.98 eV. A shift towards higher energy and a narrowing of the linewidth can be observed with decreasing temperature for the PL related peak while the Raman peak of graphene is not shifting. The area under the PL is temperature independent suggesting that the peak becoming more prominent is due to the reduced FWHM at low temperatures. Figure 3(b) shows the PL spectrum recorded at 4 K with a maximum at  $E = 1.945$  eV together with a lineshape analysis. The narrow width of 18 meV of the PL points towards a long excitonic lifetime at low temperatures.

Next, we consider the relation between the CB-VB separation from ARPES of doped  $\text{MoS}_2$  (1.976 eV) and the PL peak (1.945 eV). Naively (assuming that the Li doping does not affect the band gap value) one might expect that the difference between these two values (30 meV) is equal to the exciton binding energy. However, considering that the bandgap is related to the dielectric function and that doping leads to better screening, we expect a decrease of the bandgap. This has been observed for carbon nanotubes [28, 29] and graphene nanoribbons [30] and theoretically calculated for TMDCs [31, 32]. According to quasiparticle calculations, the band gap renormalization due to doping is expected to be the dominant factor that needs to be considered for the determination of exciton binding energies out of such an experiment. For example, for the present carrier concentration of  $3.2 \times 10^{13}$  carriers per  $\text{cm}^2$  a band gap reduction

by 450 meV is predicted [32]. Ignoring this effect would therefore only yield a lower bound of the exciton binding energy. However, if we include the calculated reduction of the ARPES band gap by doping (450 meV), we can estimate an exciton binding energy of about 480 meV. Indeed, this value is very similar to related experiments. Ugeda et al. found an exciton binding energy of 550 meV for  $\text{MoSe}_2$  on bilayer graphene on 6H-SiC(0001) by comparing PL and STS data [33]. A recent study combining ARPES and inverse photoemission of the  $\text{MoS}_2/\text{Au}$  system by Park et al. found an exciton binding energy of 90 meV [34]. This value is considerably lower because of better screening on Au and highlights the important role of the dielectric environment. Furthermore, a decrease in the band gap upon photodoping has also been observed [35].

The appearance of PL is surprising because one would expect exciton quenching by the graphene or the metallic substrate by either Förster or Dexter transfer processes [14]. Electroluminescence of monolayer  $\text{MoS}_2$  on a gold surface has been observed previously [36] by tunneling electrons directly into the  $\text{MoS}_2$  via an STM tip. Experimentally it is known that the interaction between graphene and  $\text{MoS}_2$  or semiconducting quantum dots results in luminescence quenching [14, 37, 38]. To the best of our knowledge there is no theoretical study of the mechanism of exciton quenching in the present system. However, a theoretical study of exciton quenching of luminescent molecules on graphene [39] suggests that both Förster and Dexter processes are relevant and graphene is an efficient energy sink. We speculate that the same is true for the present system.

The efficiency of luminescence quenching in exfoliated  $\text{MoS}_2/\text{Gr}$  heterostructures is reduced by the intercalation of adsorbates into the interface [14]. In the present case however, we can rule out such effects because we keep the sample always in either  $\text{N}_2$  or high vacuum (samples were carried from the growth chamber to the UHV PL/Raman system in a vacuum suitcase or a vacuum tight  $\text{N}_2$  container). The transferred samples still show a LEED pattern and the apparent height of the  $\text{MoS}_2$  islands in STM is unchanged. Therefore, we believe that intercalation of adsorbates into the  $\text{MoS}_2/\text{Gr}$  interface is not responsible for the appearance of PL. Instead, we suspect that the key for PL observation is the relatively weak graphene- $\text{MoS}_2$  interaction as already discussed in the context of XPS and ARPES data analysis. To learn more about this interaction, we show temperature dependent Raman spectroscopy data taken inside UHV in the next section.

### 2.3. Vibrational properties and strain

Raman spectra have been taken in the same experimental setup as the PL measurements inside a vacuum better than  $2 \times 10^{-10}$  mbar (see Methods). Figure 4(a) shows an overview Raman spectrum taken at 4 K using a 442 nm excitation. The  $\text{MoS}_2$  related phonons with  $A_{1g}$  and  $E_{2g}$  symmetry are strong in intensity compared to graphene (see inset of Figure 4(a)) and have a splitting of  $21 \text{ cm}^{-1}$ . A comparison of  $G$  band Raman spectra for 442 nm and 532 nm excitation is shown in Figure 4(b). A shoul-



**Table 1.** The frequency of the  $E_{2g}$  and  $A_{1g}$  is denoted by  $\omega$ ,  $\chi$  denotes the change of phonon frequency with temperature and  $\gamma$  the Grüneisen parameter.<sup>a</sup> This work MoS<sub>2</sub>/Gr/Ir(111) measured at RT.<sup>b</sup> Lee et al. exfoliated MoS<sub>2</sub> on SiO<sub>2</sub> [40].<sup>c</sup> Rice et al. [41] have determined  $\omega$  on a polymer and  $\gamma$  from four point bending.<sup>d</sup> Sahoo et al. [42] have determined  $\omega$  on SiO<sub>2</sub> and  $\chi$  between 80 K–473 K.<sup>e</sup> Najemaei et al. [43] have determined  $\chi$  in the range 300 K–500 K.<sup>f</sup> Yan et al. [44] have performed measurements of  $\chi$  for suspended monolayers and found that  $\chi$  for sapphire supported monolayer is similar.<sup>g</sup> Sugai et al. [45]

Mode	$\omega[\text{cm}^{-1}]$	$\chi[\text{cm}^{-1}/\text{K}]$	$\gamma$ (ML)	$\gamma$ (bulk)
$A_{1g}$	405.1 <sup>a</sup> , 403.0 <sup>b</sup> , 402.4 <sup>c</sup> , 408.4 <sup>d</sup> , 405.0 <sup>e</sup>	-0.013 <sup>f</sup> , -0.0123 <sup>d</sup> , -0.0143 <sup>e</sup>	0.21 <sup>c</sup>	0.21 <sup>g</sup>
$E_{2g}$	384.1 <sup>a</sup> , 384.5 <sup>b</sup> , 385.3 <sup>c</sup> , 382.6 <sup>d</sup> , 385.0 <sup>e</sup>	-0.011 <sup>f</sup> , -0.0132 <sup>d</sup> , -0.0179 <sup>e</sup>	0.65 <sup>c</sup>	0.42 <sup>g</sup>

[RAG] This image shows several Raman spectroscopy measurements of graphene and related materials. Raman spectroscopy is a technique that uses light scattering to probe the vibrational modes of molecules, providing information about their structure and composition. The graphs display intensity (arbitrary units, a.u.) versus Raman shift ( $\text{cm}^{-1}$ ), which is a measure of the energy difference between the incident and scattered light. A higher Raman shift indicates a higher energy vibrational mode. Here's a breakdown of each panel:

<sup>a</sup> "b. Broadband Raman Spectrum" This panel shows a broad Raman spectrum obtained using a 442 nm laser. It displays two prominent peaks:

<sup>c</sup> "E<sub>2g</sub> and A<sub>1g</sub> Peaks" (around 400  $\text{cm}^{-1}$ ) This peak is characteristic of graphene and indicates the in-plane vibrational mode of the carbon atoms.

<sup>d</sup> "Acoustic Phonon" (around 1500  $\text{cm}^{-1}$ ) This peak is also characteristic of graphene, representing the out-of-plane vibrational mode.

The inset shows a zoomed-in view of the region around 1500-1700  $\text{cm}^{-1}$ , highlighting the G and D peaks of graphene (more detail in panel (c)), and a peak for O<sub>2</sub> (molecular oxygen).

<sup>e</sup> "Comparison of 442 nm and 532 nm Excitation" This panel compares Raman spectra obtained using 442 nm and 532 nm laser excitation. Both show the G and D' peaks of graphene. The G peak is the main characteristic peak of graphene, and D' is a defect-related peak. The difference in excitation wavelengths affects the relative intensities of the peaks. Oxygen peaks (O<sub>2</sub>) are also visible.

<sup>f</sup> "G peak" Corresponds to the in-plane vibrational mode of sp<sup>2</sup> hybridized carbon atoms in graphene.

<sup>g</sup> "D' peak" Represents the defect-related mode of graphene. Its intensity is related to the level of defects or disorder in the graphene structure.

<sup>h</sup> "Raman Spectra on Ir(111) Substrate" This panel shows Raman spectra obtained using a 325 nm laser. Two curves are overlaid:

<sup>i</sup> "E<sub>2g</sub> and A<sub>1g</sub> Peaks" This shows the spectrum of exfoliated graphene (MoS<sub>2</sub>) grown on graphene, which is itself grown on an iridium (Ir) (111) substrate.

<sup>j</sup> "G and D' Peaks" This shows the spectrum of graphene on the Ir(111) substrate.

The peaks are in the G band region of graphene and are influenced by the interaction between graphene and the MoS<sub>2</sub> and Ir(111) substrates.

<sup>k</sup> "Temperature Dependence of Raman Spectrum" This panel shows Raman spectra taken at room temperature (RT) and 4 K (very low temperature) using 532 nm excitation. Multiple overlaid spectra are shown for each temperature, indicating measurements at multiple locations. The main focus is on the E<sub>2g</sub>-G and A<sub>1g</sub>-G peaks. The shift and broadening of these peaks with temperature are being investigated.

<sup>l</sup> "Peak Position Summary" This panel summarizes the peak positions of E<sub>2g</sub>-G and A<sub>1g</sub>-G peaks at RT and 4 K from multiple measurements (Spot #). This data visualizes the variations in peak positions observed in panel (k). It indicates that there is some variability in the peak positions across different sample locations.

In summary, the figure shows a detailed Raman spectroscopic analysis of graphene, focusing on its structural characteristics, defects, and the influence of temperature and substrate interactions. The use of different laser excitation wavelengths provides complementary information. This study aims to understand the properties of graphene and its interaction with other materials, including MoS<sub>2</sub> and Ir(111) substrates.

[RAG]

**Figure 4.** Ultra-high vacuum Raman spectroscopy of MoS<sub>2</sub>/Gr/Ir(111). (a) Overview scan at 4K using 442 nm wavelength laser. The  $A_{1g}$  and  $E_{2g}$  Raman active modes of MoS<sub>2</sub> are very strong compared to the graphene related modes. The peak at 1555  $\text{cm}^{-1}$  is due to the vibrations of molecular O<sub>2</sub> in the beam path outside of the UHV chamber. The inset shows the region around 1600  $\text{cm}^{-1}$  with the graphene G peak. (b)  $D'$  peak measurements at room temperature for 532 nm and 442 nm excitation show that the  $D'$  intensity is lower for the smaller wavelength. The small peaks around the O<sub>2</sub> vibrational peak are the rotational states of O<sub>2</sub> which are more pronounced for visible light excitation than UV. (c) Comparison of the room temperature G-peak position of MoS<sub>2</sub>/Gr/Ir(111) and Gr/Ir(111) shows a shift from 1593.4  $\text{cm}^{-1}$  to 1613.1  $\text{cm}^{-1}$ . (d) Temperature dependence of the MoS<sub>2</sub> Raman modes using a 532 nm laser at eight different spots on the sample. (e) Peak positions from Lorentzian fits to the data shown in (d). Their average values at 4 K are  $\omega_{E_{2g}} = 386.6 \text{ cm}^{-1}$  and  $\omega_{A_{1g}} = 407.8 \text{ cm}^{-1}$  and at RT the average values  $\omega_{E_{2g}} = 384.1 \text{ cm}^{-1}$  and  $\omega_{A_{1g}} = 405.1 \text{ cm}^{-1}$ .

der at  $\sim 1650 \text{ cm}^{-1}$  can be identified which is attributed to the  $D'$  band because its intensity is changing with laser energy [46, 47], as one can see from Figure 4(b). The appearance of the  $D'$  Raman band is ascribed to translational symmetry breaking by

the MoS<sub>2</sub> islands (see the STM image in Figure 1(a)) which act as scattering centers for graphene electrons. Importantly, the graphene *G* band prior to MoS<sub>2</sub> synthesis is not visible by 442 nm and 532 nm excitation. [48] However, it can be detected using UV excitation (325nm). The comparison of UV Raman spectra for Gr/Ir(111) and the MoS<sub>2</sub>/Gr/Ir(111) heterostructure are shown in Figure 4(c). A shift of *G* band position from 1593 cm<sup>-1</sup> (Gr/Ir) to 1613 cm<sup>-1</sup> (MoS<sub>2</sub>/Gr/Ir) can be seen. The frequency upshift by 20 cm<sup>-1</sup> can be explained by two effects that take place after growth of MoS<sub>2</sub>. First, graphene becomes p-doped (that we have analyzed by ARPES). The *G* band frequency upshift upon p-doping has been reported in the literature. [49, 50, 51, 48] For the observed hole concentration of  $1.48 \times 10^{13}$  cm<sup>-2</sup> an upshift from the position of charge neutral graphene by  $\sim 18$  cm<sup>-1</sup> is predicted. [50] Neglecting the small initial p-doping of Gr/Ir(111), this is in very good agreement to the observed 20 cm<sup>-1</sup> upshift. Notably, the precise value of the upshift depends also on the substrate and other works report values in the range of  $\sim 5$ -10 cm<sup>-1</sup> (Refs. [49, 51, 48]). Second, we believe that, after MoS<sub>2</sub> growth, Gr on Ir(111) becomes flatter which leads to compressive strain in Gr. This is corroborated by the fact that the Gr/Ir(111) moiré spots in the LEED pattern become weaker after MoS<sub>2</sub> growth. The wavyness of the moiré can help to relax some of the strain in the Gr/Ir(111) system. However, after MoS<sub>2</sub> growth, as Gr becomes flatter, it also acquires compressive strain which is known to cause an upshift in the *G* band frequency [49, 52].

Let us now move to the investigation of temperature induced strain in the heterostructure. Raman spectroscopy is a well suited tool to investigate the change of bond length due to strain via the frequency change of Raman active vibrations. The information of that frequency change versus temperature yields information on how strongly bonded graphene and MoS<sub>2</sub> are to each other and to the substrate. For example, if both layers would follow the thermal expansion of the Ir substrate, we can assume that they are strongly bonded to each other. For graphene which is in direct contact to the Ir surface and fully covering it, one might expect that the C-C bond length follows the thermal expansion of the bulk Ir. However, the situation of MoS<sub>2</sub> is less obvious because it is not in direct contact to the Ir and not a complete monolayer which can make it easier to maintain a thermal expansion coefficient of its own. Figure 4(d) depicts scans at several spots on the sample performed at RT and at 4 K. It can be seen that, upon cooling the phonons harden by 2.7 cm<sup>-1</sup> (the A<sub>1g</sub> mode) and by 2.6 cm<sup>-1</sup> (the E<sub>2g</sub> mode). The temperature dependent phonon frequency is phenomenologically described as  $\Delta\omega = \chi\Delta T$  where  $\Delta\omega$  is the frequency shift and  $\chi$  is a phonon shift per Kelvin. For MoS<sub>2</sub> there is a consensus in the literature that  $\chi \sim -0.01$  cm<sup>-1</sup>/K [42, 53, 54] (see Table 1). Interestingly, this number is largely independent of the substrate and holds also for freestanding layers [44]. It is approximately the same for both A<sub>1g</sub> and E<sub>2g</sub> phonon modes. Plugging in  $\Delta T \sim 290$  K, we would expect a shift by  $\Delta\omega = 3.5$  cm<sup>-1</sup> for freestanding MoS<sub>2</sub> which is close to explaining the experimental value, but not in perfect agreement with the measured 2.6 cm<sup>-1</sup>. Considering alternative scenarios,

the other extremum is strongly substrate bound MoS<sub>2</sub>. In this case, the phonon shift is dictated by the temperature induced substrate strain  $\epsilon$  caused by the change of the substrate lattice parameter, to which MoS<sub>2</sub> would be pinned. This strain can be derived from the linear thermal expansion coefficient of iridium [55, 56]. We proceed by first applying this analysis to the graphene  $G$  band and then to MoS<sub>2</sub>. The strain  $\epsilon$  and the phonon shift  $\Delta\omega$  are linked to each other via the Grüneisen parameter  $\gamma$  and the phonon mode degeneracy  $n$  as  $\Delta\omega = \epsilon n \gamma \omega_0$ . Here  $\omega_0$  is the phonon frequency of the unstrained system. The temperature induced strain  $\epsilon$  for the Ir substrate yields  $\epsilon = 0.134\%$ . Plugging this into the above equation for the graphene  $G$  mode with  $E_{2g}$  symmetry and using  $\omega_0 = 1593.2 \text{ cm}^{-1}$ ,  $n = 2$   $\gamma = 2$ , we obtain  $\omega = 1604.1 \text{ cm}^{-1}$  (in Ref. [48] this analysis has been performed for the first time for Gr/Ir(111) and more details can be found there). Importantly, the temperature dependent upshift in  $\omega$  upon cooling for the  $G$  band is in good agreement to the experiment. This implies that graphene is pinned to the Ir substrate [48].

Performing the same estimation for MoS<sub>2</sub> we try to obtain a value for the temperature dependent phonon energy shift. The Grüneisen parameters of monolayer MoS<sub>2</sub> are reported in the literature as  $\gamma_{A_{1g}} = 0.21$  and  $\gamma_{E_{2g}} = 0.65$  (Ref. [41]). If we now apply the above formula, assuming that  $\epsilon$  is that of the strained Ir substrate, we find  $\Delta\omega_{A_{1g}} = 0.11 \text{ cm}^{-1}$  and  $\Delta\omega_{E_{2g}} = 0.67 \text{ cm}^{-1}$ . This does not agree with experiment at all. Notably, also using the Grüneisen parameter of bulk MoS<sub>2</sub> ( $\gamma_{A_{1g}} = 0.21$  and  $\gamma_{E_{2g}} = 0.42$  from Ref. [45]) would not improve agreement. We thus conclude that MoS<sub>2</sub> does not follow the thermal expansion of Ir and its behaviour is better described by the expansion expected for a freestanding monolayer. Graphene, however, is stronger interacting with the Ir substrate and its Raman shift as a function of temperature can be fully understood by the thermal expansion of the substrate.

### 3. Conclusion and Outlook

We have characterized the epitaxially grown MoS<sub>2</sub>/Gr/Ir(111) system combining XPS, ARPES, Raman and PL measurements. STM, LEED and XPS confirm the good quality of our grown samples. We have observed a PL-signal with small FWHM suggesting a long excitonic lifetime. This surprising result is the first clear observation of photoluminescence of epitaxially grown MoS<sub>2</sub> on a metallic substrate. The absence of the expected quenching of the PL intensity on a metallic surface can potentially be explained by a weak interaction between the epitaxial MoS<sub>2</sub> and the substrate as is suggested by our XPS, ARPES and temperature dependent Raman measurements. Using Li deposition, we induced doping of MoS<sub>2</sub> into a degenerate semiconductor and obtained from the analysis of ARPES data the band gap of Li-doped MoS<sub>2</sub>. Using theoretical calculations on the band gap renormalization due to doping, we estimate an exciton binding energy of 480 meV. Our results suggest that the MoS<sub>2</sub>-islands are only weakly interacting with the Gr/Ir surface which could explain the absence of quenching, but the microscopic mechanisms are still unclear. Theoretical calculations for the Dexter-

and Förster-type energy transfer from the islands into the graphene substrate are thus needed to quantitatively explain the observed PL. With this background it would be interesting to grow  $\text{MoS}_2$  on hexagonal boron nitride (h-BN) using the same method as used for this work and compare FWHM and intensity of the PL. Indeed, previous experiments on h-BN capped  $\text{MoS}_2$  [8] have shown an increase in the PL intensity upon h-BN encapsulation. Similarly, it was shown that chemical treatment of  $\text{MoS}_2$  flakes via an organic superacid increased PL quantum yield to near unity [57], similar treatment of epitaxially grown  $\text{MoS}_2$  monolayers might increase PL intensity even more. Additionally a transfer of  $\text{MoS}_2$  islands grown on Gr/ $\text{Ir}(111)$  onto different substrates could help to understand the effects of the substrate on the luminescent properties.

#### 4. Appendix / supporting information

[ARPES] The image shows two grayscale plots, both presenting band structures. These are likely experimental data from angle-resolved photoemission spectroscopy (ARPES) or a similar technique used to measure the electronic band structure of a material.

Top Plot:

- Top axis: "Wavevector (Å<sup>-1</sup>)". This represents the momentum of electrons in the material. The scale ranges from approximately 0 to 1.7 Å<sup>-1</sup>.
- Left axis: "Binding Energy (eV)". This represents the energy required to remove an electron from the material. The scale ranges from 0 to 3.4 eV. 0 eV represents the Fermi level (the highest occupied energy level at absolute zero temperature). Higher binding energies mean the electrons are more tightly bound to the material.
- Color: The grayscale represents the intensity of photoelectrons detected at each wavevector and binding energy. Brighter regions indicate a higher density of states (more electrons at that energy and momentum).
- Annotations: "A" and "B" are points in a region labeled "Dirac bands". This suggests the plot shows the electronic bands of a bilayer material (a material consisting of two atomic layers). The specific features pointed out are likely characteristic of the electronic structure of such a bilayer material.

Bottom Plot:

- Top axis: "Wavevector (Å<sup>-1</sup>)", similar to the top plot.
- Left axis: "Binding Energy (eV)", similar to the top plot.
- Color: This plot is also a grayscale representation of the intensity of photoelectrons. It shows a band structure, likely of the same material, but potentially under different conditions (temperature, doping, etc.) or with a different measurement technique with a different resolution. The bands appear more clearly defined.
- Key Difference: The bottom plot shows a more detailed and resolved band structure compared to the top plot, suggesting better resolution or different measurement conditions.

Overall Interpretation:

The two plots likely show the band structure of a bilayer material measured under different conditions or using different techniques. The top plot may show a less well-resolved structure, possibly due to limitations in the measurement, while the bottom plot provides a more refined view of the bilayer bands. The goal is to understand the energy dispersion relation of the electrons within the material, which is crucial for understanding its electronic properties and potential applications.

[ARPES]

**Figure 5.** ARPES of bilayer  $\text{MoS}_2/\text{Gr}$ . Upper panel: raw data, lower panel: second derivative for enhancing spectral features.

##### 4.1. ARPES of bilayer $\text{MoS}_2$

Figure 5 depicts ARPES spectra of bilayer  $\text{MoS}_2$  that has been grown by doubling the deposited amount of Mo. This resulted in 1.4 monolayers (ML) of  $\text{MoS}_2$  but growth

conditions were specifically tuned to induce bilayer growth via sulfur pressure in the chamber and cycled growth (see Methods section). It is clear from ARPES that the VB maximum is not at the  $K$  point but at the  $\Gamma$  point (note the splitting of the band at  $\Gamma$  into two subbands, one with a higher binding energy of approximately 1.9 eV and one with a lower binding energy of approximately 1.3 eV).

## 5. Methods

### 5.1. X-ray photoemission spectroscopy

XPS was performed at the German-Russian beamline (RGLB) of the HZB BESSY II synchrotron in Berlin (Germany) with a beam energy of 650 eV and pass energy of 20 eV in a normal emission geometry. The  $\text{MoS}_2/\text{Gr}/\text{Ir}(111)$  samples were prepared in-situ and measured in a vacuum better than  $5 \times 10^{-10}$  mbar.

### 5.2. Angle-resolved photoemission spectroscopy

ARPES was performed at the BaDElPh beamline [58] of the Elettra synchrotron in Trieste (Italy) with linear s- and p- polarisation at  $h\nu = 31$  eV at temperatures of 20 K. The  $\text{MoS}_2/\text{Gr}/\text{Ir}(111)$  samples were prepared in-situ and measured in a vacuum better than  $5 \times 10^{-11}$  mbar. Li deposition was carried out in an ultra-high vacuum (UHV) chamber from SAES getters with the sample at 20 K. We performed stepwise evaporation of Li which we monitored by ARPES measurements of the band structure. Li evaporation was stopped after the desired doping level was reached.

### 5.3. Scanning Tunneling Spectroscopy and Microscopy

Scanning tunneling microscopy was conducted in a home built variable temperature STM apparatus in Cologne at a base pressure below  $8 \times 10^{-11}$  mbar. For image processing the software WSxM was used [59].

### 5.4. Growth

We employ molecular beam epitaxy via a two-step process [13]: In the first step, with the sample held at room temperature, Mo is evaporated at a rate of  $\approx 1.4 \times 10^{16}$  atoms  $\text{m}^{-2} \text{s}^{-1}$  into a S background pressure of  $p \approx 5 \times 10^{-9}$  mbar onto  $\text{Gr}/\text{Ir}(111)$ . The elemental S background atmosphere is achieved by heating a pyrite ( $\text{FeS}_2$ ) filled crucible to  $\approx 500$  K. During the second step, the sample is annealed for 300 s at  $T = 1050$  K in a S pressure of  $p \approx 2 \times 10^{-9}$  mbar. These two steps constitute one growth cycle.

To obtain a  $\text{MoS}_2$  layer with orientation epitaxy even for coverages beyond 0.4 ML the total coverage was deposited in subsequent growth cycles each yielding a coverage of  $\approx 0.35$  ML  $\text{MoS}_2$ . Using this technique we realized two cycle  $\text{MoS}_2$  samples (nominal

coverage 0.7 ML) and four cycle MoS<sub>2</sub> samples (nominal coverage 1.4 ML).

### 5.5. Ultra-high Vacuum Raman and photoluminescence spectroscopy

UHV Raman measurements were performed in the back-scattering geometry using commercial Raman systems (Renishaw) integrated in a homebuilt optical chamber [27], where the exciting and Raman scattered light were coupled into the vacuum using a 50x long-working distance microscope objective with an NA of  $\sim 0.4$  and a focal distance of 20.5 mm for lasers with wavelength 442 nm and 532 nm. For the UV laser, a UV compatible microscope objective has been used. The 20x UV objective has a focal distance equal to 13 mm and an NA=0.32. A sketch of our experimental setup is shown in a previous work [27]. Power densities in the range of 100 kW/cm<sup>2</sup> have been employed for all laser energies. The position of the laser on the sample could be checked by a camera in the laser path. All spectra have been calibrated in position and intensity to the O<sub>2</sub> vibration at 1555 cm<sup>-1</sup> [60].

## 6. Acknowledgements

N.E., J.H., A.H., T.M. and A.G. acknowledge support through the CRC 1238 within project A01. N.E., B.V.S., M.H. and A.G. acknowledge the ERC grant no. 648589 'SUPER-2D' and funding from DFG projects GR 3708/2-1. A.G. acknowledges INST 216/808-1 FUGG and support from the "Quantum Matter and Materials" (QM2) initiative. N.E., M.H., J.L and A.G. acknowledge support from CALIPSOplus and CERIC-ERIC for their stay at ELETTRA sincrotrone.

## References

- [1] Kin Fai Mak, Changgu Lee, James Hone, Jie Shan, and Tony F. Heinz. Atomically thin MoS<sub>2</sub>: A new direct-gap semiconductor. *Physical Review Letters*, 105:136805, 2010.
- [2] Sajede Manzeli, Dmitry Ovchinnikov, Diego Pasquier, Oleg V. Yazyev, and Andras Kis. 2D transition metal dichalcogenides. *Nature Reviews Materials*, 2:17033–, June 2017.
- [3] Gang Wang, Alexey Chernikov, Mikhail M. Glazov, Tony F. Heinz, Xavier Marie, Thierry Amand, and Bernhard Urbaszek. Excitons in atomically thin transition metal dichalcogenides. *Reviews of Modern Physics*, 90(2):21001, 2017.
- [4] Manish Chhowalla, Hyeon Suk Shin, Goki Eda, Lain-Jong Li, Kian Ping Loh, and Hua Zhang. The chemistry of two-dimensional layered transition metal dichalcogenide nanosheets. *Nature Chemistry*, 5:263–, March 2013.
- [5] B. Radisavljevic, A. Radenovic, J. Brivio, V. Giacometti, and A. Kis. Single-layer MoS<sub>2</sub> transistors. *Nature Nanotechnology*, 6:147–, January 2011.
- [6] Der-Hsien Lien, Matin Amani, Sujay B. Desai, Geun Ho Ahn, Kevin Han, Jr-Hau He, Joel W. Ager, Ming C. Wu, and Ali Javey. Large-area and bright pulsed electroluminescence in monolayer semiconductors. *Nature Communications*, 9(1):1229, 2018.
- [7] Jonghwan Kim, Chenhao Jin, Bin Chen, Hui Cai, Tao Zhao, Puiyee Lee, Salman Kahn, Kenji Watanabe, Takashi Taniguchi, Sefaattin Tongay, Michael F. Crommie, and Feng Wang.

- Observation of ultralong valley lifetime in  $\text{WSe}_2/\text{MoS}_2$  heterostructures. *Science Advances*, 3(7), 2017.
- [8] F. Cadiz, E. Courtade, C. Robert, G. Wang, Y. Shen, H. Cai, T. Taniguchi, K. Watanabe, H. Carrere, D. Lagarde, M. Manca, T. Amand, P. Renucci, S. Tongay, X. Marie, and B. Urbaszek. Excitonic linewidth approaching the homogeneous limit in  $\text{MoS}_2$ -based van der Waals heterostructures. *Physical Review X*, 7(2):1–12, 2017.
  - [9] Signe S. Grønberg, Søren Ulstrup, Marco Bianchi, Maciej Dendzik, Charlotte E. Sanders, Jeppe V. Lauritsen, Philip Hofmann, and Jill A. Miwa. Synthesis of Epitaxial Single-Layer  $\text{MoS}_2$  on  $\text{Au}(111)$ . *Langmuir*, 31:9700, 2015.
  - [10] Harsh Bana, Elisabetta Travaglia, Luca Bignardi, Paolo Lacovig, Charlotte E Sanders, Maciej Dendzik, Matteo Michiardi, Marco Bianchi, Daniel Lizzit, Francesco Presel, Dario De Angelis, Nicoleta Apostol, Pranab Kumar Das, Jun Fujii, Ivana Vobornik, Rosanna Larciprete, Alessandro Baraldi, Philip Hofmann, and Silvano Lizzit. Epitaxial growth of single-orientation high-quality  $\text{MoS}_2$  monolayers. *2D Materials*, 5:035012, 2018.
  - [11] Jill A. Miwa, Søren Ulstrup, Signe G. Sørensen, Maciej Dendzik, Antonija Grubišić Čabo, Marco Bianchi, Jeppe Vang Lauritsen, and Philip Hofmann. Electronic structure of epitaxial single-layer  $\text{MoS}_2$ . *Physical Review Letters*, 114(4):1–5, 2015.
  - [12] Deyi Fu, Xiaoxu Zhao, Yu-Yang Zhang, Linjun Li, Hai Xu, A-Rang Jang, Seong In Yoon, Peng Song, Sock Mui Poh, Tianhua Ren, Zijing Ding, Wei Fu, Tae Joo Shin, Hyeon Suk Shin, Sokrates T. Pantelides, Wu Zhou, and Kian Ping Loh. Molecular beam epitaxy of highly crystalline monolayer molybdenum disulfide on hexagonal boron nitride. *Journal of the American Chemical Society*, 139(27):9392–9400, 2017.
  - [13] Joshua Hall, Borna Piel, Clifford Murray, Wouter Jolie, Tobias Wekking, Carsten Busse, Marko Kralj, and Thomas Michely. Molecular beam epitaxy of quasi-freestanding transition metal disulphide monolayers on van der waals substrates: a growth study. *2D Materials*, 5(2):025005, 2018.
  - [14] Guillaume Froehlicher, Etienne Lorchat, and Stéphane Berciaud. Charge Versus Energy Transfer in Atomically Thin Graphene-Transition Metal Dichalcogenide van der Waals Heterostructures. *Physical Review X*, 8(1):1–15, 2018.
  - [15] Wouter Jolie, Clifford Murray, Phillip S. Weiß, Joshua Hall, Fabian Portner, Nicolae Atodiresei, Arkady V. Krasheninnikov, Carsten Busse, Hannu-Pekka Komsa, Achim Rosch, and Thomas Michely. Luttinger liquid in a box: electrons confined within  $\text{mos}_2$  mirror twin boundaries. *not yet published*, 2018.
  - [16] P A Young. Lattice parameter measurements on molybdenum disulphide. *Journal of Physics D: Applied Physics*, 1(7):936–938, 1968.
  - [17] Albert Bruix, Henrik Gøbel Flichtbauer, Anders K. Tuxen, Alexander S. Walton, Mie Andersen, Søren Porsgaard, Flemming Besenbacher, Bjørk Hammer, and Jeppe V. Lauritsen. In situ detection of active edge sites in single-layer  $\text{MoS}_2$  catalysts. *ACS Nano*, 9(9):9322–9330, 2015.
  - [18] Hernan G. Sanchez Casalongue, Jesse D. Benck, Charlie Tsai, Rasmus K. B. Karlsson, Sarp Kaya, May Ling Ng, Lars G. M. Pettersson, Frank Abild-Pedersen, J. K. Nørskov, Hirohito Ogasawara, Thomas F. Jaramillo, and Anders Nilsson. Operando characterization of an amorphous molybdenum sulfide nanoparticle catalyst during the hydrogen evolution reaction. *The Journal of Physical Chemistry C*, 118(50):29252–29259, nov 2014.
  - [19] Marko Kralj, Ivo Pletikosić, Marin Petrović, Petar Pervan, Milorad Milun, Alpha T. N'Diaye, Carsten Busse, Thomas Michely, Jun Fujii, and Ivana Vobornik. Graphene on  $\text{ir}(111)$  characterized by angle-resolved photoemission. *Physical Review B*, 84(7), 2011.
  - [20] I. Pletikosić, M. Kralj, P. Pervan, R. Brako, J. Coraux, A. T. N'Diaye, C. Busse, and T. Michely. Dirac cones and minigaps for graphene on  $\text{Ir}(111)$ . *Physical Review Letters*, 102:056808, Feb 2009.
  - [21] Elena Starodub, Aaron Bostwick, Luca Moreschini, Shu Nie, Farid El Gabaly, Kevin F. McCarty, and Eli Rotenberg. In-plane orientation effects on the electronic structure, stability, and raman

- scattering of monolayer graphene on  $\text{Ir}(111)$ . *Physical Review B*, 83(12), mar 2011.
- [22] D. Nasr Esfahani, O. Leenaerts, H. Sahin, B. Partoens, and F. M. Peeters. Structural transitions in monolayer  $\text{MoS}_2$  by lithium adsorption. *J. Phys. Chem. C*, 119(19):10602–10609, May 2015.
  - [23] Yuanliao Zheng, Yan Huang, Haibo Shu, Xiaohao Zhou, Jiayi Ding, Xiaoshuang Chen, and Wei Lu. The effect of lithium adsorption on the formation of 1T- $\text{MoS}_2$  phase based on first-principles calculation. *Physics Letters A*, 380(20):1767–1771, apr 2016.
  - [24] Wenshu Chen, Jiajun Gu, Qinglei Liu, Ruichun Luo, Lulu Yao, Boya Sun, Wang Zhang, Huilan Su, Bin Chen, Pan Liu, and Di Zhang. Quantum dots of 1T phase transitional metal dichalcogenides generated via electrochemical Li intercalation. *ACS Nano*, 12(1):308–316, 2018.
  - [25] Hai He, Pengfei Lu, Liyuan Wu, Chunfang Zhang, Yuxin Song, Pengfei Guan, and Shumin Wang. Structural properties and phase transition of Na adsorption on monolayer  $\text{MoS}_2$ . *Nanoscale Research Letters*, 11(1), 2016.
  - [26] T. Eknapakul, P. D. C. King, M. Asakawa, P. Buaphet, R.-H. He, S.-K. Mo, H. Takagi, K. M. Shen, F. Baumberger, T. Sasagawa, S. Junghwan, and W. Meevasana. Electronic structure of a quasi-freestanding  $\text{MoS}_2$  monolayer. *Nano Letters*, 14(3):1312–1316, March 2014.
  - [27] A. Grüneis, B.V. Senkovskiy, A.V. Fedorov, M. Hell, and S. Michel. Ultrahigh vacuum optical spectroscopy of chemically functionalized graphene nanoribbons. In *Reference Module in Chemistry, Molecular Sciences and Chemical Engineering*, pages –. Elsevier, 2017.
  - [28] Catalin D. Spataru and François Léonard. Tunable band gaps and excitons in doped semiconducting carbon nanotubes made possible by acoustic plasmons. *Physical Review Letters*, 104:177402, Apr 2010.
  - [29] Holger Hartleb, Florian Späth, and Tobias Hertel. Evidence for strong electronic correlations in the spectra of gate-doped single-wall carbon nanotubes. *ACS Nano*, 9(10):10461–10470, 2015. PMID: 26381021.
  - [30] Boris V. Senkovskiy, Alexander V. Fedorov, Danny Haberer, Mani Farjam, Konstantin A. Simonov, Alexei B. Preobrajenski, Niels Mårtensson, Nicolae Atodiresei, Vasile Caciuc, Stefan Blügel, Achim Rosch, Nikolay I. Verbitskiy, Martin Hell, Daniil V. Evtushinsky, Raphael German, Tomas Marangoni, Paul H. M. van Loosdrecht, Felix R. Fischer, and Alexander Grüneis. Semiconductor-to-metal transition and quasiparticle renormalization in doped graphene nanoribbons. *Adv. Electron. Mater.*, 3(4):1600490, 2017.
  - [31] Shiyuan Gao, Yufeng Liang, Catalin D. Spataru, and Li Yang. Dynamical excitonic effects in doped two-dimensional semiconductors. *Nano Letters*, 16(9):5568–5573, September 2016.
  - [32] Yufeng Liang and Li Yang. Carrier plasmon induced nonlinear band gap renormalization in two-dimensional semiconductors. *Physical Review Letters*, 114:063001, Feb 2015.
  - [33] Miguel M. Ugeda, Aaron J. Bradley, Su-Fei Shi, Felipe H. da Jornada, Yi Zhang, Diana Y. Qiu, Wei Ruan, Sung-Kwan Mo, Zahid Hussain, Zhi-Xun Shen, Feng Wang, Steven G. Louie, and Michael F. Crommie. Giant bandgap renormalization and excitonic effects in a monolayer transition metal dichalcogenide semiconductor. *Nature Materials*, 13:1091–, 2014.
  - [34] Soohyung Park, Niklas Mutz, Thorsten Schultz, Sylke Blumstengel, Ali Han, Areej Aljarb, Lain-Jong Li, Emil J W List-Kratochvil, Patrick Amsalem, and Norbert Koch. Direct determination of monolayer  $\text{MoS}_2$  and  $\text{WSe}_2$  exciton binding energies on insulating and metallic substrates. *2D Materials*, 5(2):025003, 2018.
  - [35] Eva A. A. Pogna, Margherita Marsili, Domenico De Fazio, Stefano Dal Conte, Cristian Manzoni, Davide Sangalli, Duhee Yoon, Antonio Lombardo, Andrea C. Ferrari, Andrea Marini, Giulio Cerullo, and Deborah Prezzi. Photo-induced bandgap renormalization governs the ultrafast response of single-layer  $\text{MoS}_2$ . *ACS Nano*, 10(1):1182–1188, January 2016.
  - [36] Nils Krane, Christian Lotze, Julia M. Läger, Gal Reecht, and Katharina J. Franke. Electronic structure and luminescence of quasi-freestanding  $\text{MoS}_2$  nanopatches on  $\text{Au}(111)$ . *Nano Letters*, 16(8):5163–5168, 2016.
  - [37] L. Gaudreau, K. J. Tielrooij, G. E. D. K. Prawiroatmodjo, J. Osmond, F. J. Garca de Abajo, and F. H. L. Koppens. Universal distance-scaling of nonradiative energy transfer to graphene.



- Nano Letters, 13(5):2030–2035, 2013. PMID: 23488979.
- [38] Franois Federspiel, Guillaume Froehlicher, Michel Nasilowski, Silvia Pedetti, Ather Mahmood, Bernard Doudin, Serin Park, Jeong-O Lee, David Halley, Benot Dubertret, Pierre Gilliot, and Stphane Berciaud. Distance dependence of the energy transfer rate from a single semiconductor nanostructure to graphene. Nano Letters, 15(2):1252–1258, February 2015.
  - [39] Ermin Malic, Heiko Appel, Oliver T. Hofmann, and Angel Rubio. Förster-induced energy transfer in functionalized graphene. Journal of Physical Chemistry C, 118(17):9283–9289, 2014.
  - [40] Changgu Lee, Huguen Yan, Louis E. Brus, Tony F. Heinz, James Hone, and Sunmin Ryu. Anomalous lattice vibrations of single- and few-layer MoS<sub>2</sub>. ACS Nano, 4(5):2695–2700, May 2010.
  - [41] C. Rice, R. J. Young, R. Zan, U. Bangert, D. Wolverson, T. Georgiou, R. Jalil, and K. S. Novoselov. Raman-scattering measurements and first-principles calculations of strain-induced phonon shifts in monolayer MoS<sub>2</sub>. Physical Review B - Condensed Matter and Materials Physics, 87(8):1–5, 2013.
  - [42] Satyaprakash Sahoo, Anand P. S. Gaur, Majid Ahmadi, Maxime J.-F. Guinel, and Ram S. Katiyar. Temperature-dependent raman studies and thermal conductivity of few-layer MoS<sub>2</sub>. The Journal of Physical Chemistry C, 117(17):9042–9047, 2013.
  - [43] Sina Najmaei, Pulickel M. Ajayan, and J. Lou. Quantitative analysis of the temperature dependency in Raman active vibrational modes of molybdenum disulfide atomic layers. Nanoscale, 5(20):9758–9763, 2013.
  - [44] Rusen Yan, Jeffrey R. Simpson, Simone Bertolazzi, Jacopo Brivio, Michael Watson, Xufei Wu, Andras Kis, Tengfei Luo, Angela R. Hight Walker, and Huili Grace Xing. Thermal conductivity of monolayer molybdenum disulfide obtained from temperature-dependent raman spectroscopy. ACS Nano, 8(1):986–993, January 2014.
  - [45] S. Sugai and T. Ueda. High-pressure raman spectroscopy in the layered materials 2H-MoS<sub>2</sub>, 2H-MoSe<sub>2</sub>, and 2H-MoTe<sub>2</sub>. Physical Review B, 26:6554–6558, Dec 1982.
  - [46] L. G. Canado, K. Takai, T. Enoki, M. Endo, Y. A. Kim, H. Mizusaki, A. Jorio, L. N. Coelho, R. Magalhes-Paniago, and M. A. Pimenta. General equation for the determination of the crystallite size La of nanographite by Raman spectroscopy. Applied Physics Letters, 88(16):163106, 2006.
  - [47] M. A. Pimenta, G. Dresselhaus, M. S. Dresselhaus, L. G. Canado, A. Jorio, and R. Saito. Studying disorder in graphite-based systems by Raman spectroscopy. Phys. Chem. Chem. Phys., 9:1276–1290, 2007.
  - [48] Martin et al. Hell. Resonance Raman spectrum of doped epitaxial graphene at the Lifshitz transition. submitted, 2018.
  - [49] Michele Lazzeri and Francesco Mauri. Nonadiabatic kohn anomaly in a doped graphene monolayer. Physical Review Letters, 97(26):266407, 2006.
  - [50] A. Das, S. Pisana, B. Chakraborty, S. Piscanec, S. K. Saha, U. V. Waghmare, K. S. Novoselov, H. R. Krishnamurthy, A. K. Geim, A. C. Ferrari, and A. K. Sood. Monitoring dopants by raman scattering in an electrochemically top-gated graphene transistor. Nature Nanotechnology, 3:210–, March 2008.
  - [51] Chi-Fan Chen, Cheol-Hwan Park, Bryan W. Boudouris, Jason Horng, Baisong Geng, Caglar Girit, Alex Zettl, Michael F. Crommie, Rachel A. Segalman, Steven G. Louie, and Feng Wang. Controlling inelastic light scattering quantum pathways in graphene. Nature, 471:617–, March 2011.
  - [52] T. M. G. Mohiuddin, A. Lombardo, R. R. Nair, A. Bonetti, G. Savini, R. Jalil, N. Bonini, D. M. Basko, C. Galiotis, N. Marzari, K. S. Novoselov, A. K. Geim, and A. C. Ferrari. Uniaxial strain in graphene by raman spectroscopy: *g* peak splitting, Grüneisen parameters, and sample orientation. Phys. Rev. B, 79:205433, May 2009.
  - [53] Liqin Su, Yong Zhang, Yifei Yu, and Linyou Cao. Dependence of coupling of quasi 2-D MoS<sub>2</sub> with substrates on substrate types, probed by temperature dependent Raman scattering. Nanoscale,

- 6(9):4920–4927, 2014.
- [54] Tianqi Yang, Xiaoting Huang, Hong Zhou, Guangheng Wu, and Tianshu Lai. Excitation mechanism of  $A_{1g}$  mode and origin of nonlinear temperature dependence of Raman shift of CVD-grown mono- and few-layer  $\text{MoS}_2$  films. *Optics Express*, 24(11):12281, 2016.
  - [55] G. K. White and A. T. Pawlowicz. Thermal expansion of rhodium, iridium, and palladium at low temperatures. *Journal of Low Temperature Physics*, 2(5):631–639, Jun 1970.
  - [56] J. J. Halvorson and R. T. Wimber. Thermal expansion of iridium at high temperatures. *Journal of Applied Physics*, 43(6):2519–2522, 1972.
  - [57] M. Amani, D.-H. Lien, Daisuke Kiriya, J. Xiao, A. Azcatl, J. Noh, Surabhi R Madhvapathy, R. Addou, S. KC, M. Dubey, K. Cho, R. M. Wallace, S.-C. Lee, J.-H. He, J. W. Ager, X. Zhang, E. Yablonovitch, and A. Javey. Near-unity photoluminescence quantum yield in  $\text{MoS}_2$ . *Science*, 350(6264):1065–1068, 2015.
  - [58] L. Petaccia, P. Vilmercati, S. Gorovikov, M. Barnaba, A. Bianco, D. Cocco, C. Masciovecchio, and A. Goldoni. Bad elph: A normal-incidence monochromator beamline at elettra. *Nuclear Instruments and Methods in Physics Research Section A: Accelerators, Spectrometers, Detectors and Associated Equipment*, 606(3):780–784, 2009.
  - [59] I. Horcas, R. Fernandez, J.M. Gomez-Rodriguez, J. Colchero, J. Gomez-Herrero, and A.M. Baro. Wsxn: A software for scanning probe microscopy and a tool for nanotechnology. *Review of Scientific Instruments*, 78(1):013705, 2007.
  - [60] Gregory W. Faris and Richard A. Copeland. Ratio of oxygen and nitrogen raman cross sections in the ultraviolet. *Appl. Opt.*, 36(12):2684–2685, Apr 1997.